

Evidence of Redox-Active Iron Formation Following Aggregation of Ferrihydrite and the Alzheimer's Disease Peptide β -Amyloid

James Everett,^{†,☆} Eva Céspedes,[†] Leigh R. Shelford,[‡] Chris Exley,[§] Joanna F. Collingwood,[▽] Jon Dobson,^{||} Gerrit van der Laan,[○] Catherine A. Jenkins,[†] Elke Arenholz,[†] and Neil D. Telling^{*,†,☆}

[†]Institute for Science and Technology in Medicine, Keele University, Stoke-on-Trent, Staffordshire ST4 7QB, United Kingdom

[‡]College of Engineering, Mathematics and Physical Sciences, University of Exeter, Exeter EX4 4QL, United Kingdom

[§]The Birchall Centre, Lennard-Jones Laboratories, Keele University, Staffordshire ST5 5BG, United Kingdom

[▽]School of Engineering, University of Warwick, Coventry CV4 7AL, United Kingdom

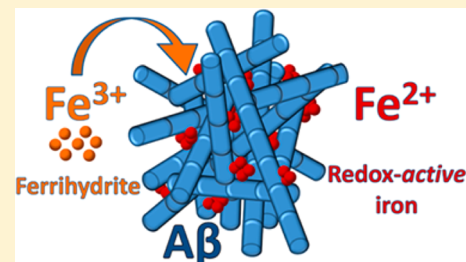
^{||}J. Crayton Pruitt Family Department of Biomedical Engineering & Department of Materials Science and Engineering, University of Florida, Gainesville, Florida 32611, United States

[○]Magnetic Spectroscopy Group, Diamond Light Source, Didcot, Oxfordshire OX11 0DE, United Kingdom

[†]Advanced Light Source, Lawrence Berkeley National Laboratory, Berkeley, California, 94720, United States

Supporting Information

ABSTRACT: Recent work has demonstrated increased levels of redox-active iron biominerals in Alzheimer's disease (AD) tissue. However, the origin, nature, and role of iron in AD pathology remains unclear. Using X-ray absorption, X-ray microspectroscopy, and electron microscopy techniques, we examined interactions between the AD peptide β -amyloid ($A\beta$) and ferrihydrite, which is the ferric form taken when iron is stored in humans. We report that $A\beta$ is capable of reducing ferrihydrite to a pure iron(II) mineral where antiferromagnetically ordered Fe^{2+} cations occupy two nonequivalent crystal symmetry sites. Examination of these iron(II) phases following air exposure revealed a material consistent with the iron(II)-rich mineral magnetite. These results demonstrate the capability of $A\beta$ to induce the redox-active biominerals reported in AD tissue from natural iron precursors. Such interactions between $A\beta$ and ferrihydrite shed light upon the processes of AD pathogenesis, while providing potential targets for future therapies.



INTRODUCTION

Alzheimer's disease (AD) is a fatal age-related neurodegenerative disorder characterized by extensive neuronal loss in the higher brain centers, resulting in cognitive decline, memory loss, and psychosis. Since this process of neurodegeneration is highly complex, AD pathology is poorly understood and no cure exists.^{1–3} However, it is becoming accepted that the accumulation of the peptide β -amyloid ($A\beta$) within neurons may be fundamental to the disease process.^{4,5} This $A\beta$ peptide forms dysfunctional protein aggregates, which are deposited extracellularly, manifesting as amyloid plaques.^{5–7} It has been suggested that areas of AD pathology, such as amyloid plaques, are correlated with increased concentrations of brain iron.^{8,9} Although iron is vital for healthy brain function,^{10,11} certain forms or excess concentrations can be toxic.^{12–14} This toxicity arises through iron's valence chemistry, enabling it to participate in Fenton chemistry, leading to the generation of toxic free radicals.^{15–17} These reactive oxygen species (ROS) go on to cause oxidative stress in the brain manifesting as neuronal injury.^{2,12,15,17}

Iron toxicity depends upon its *redox* state and normal brain iron is stored as ferrihydrite, which is a *redox-inactive* iron(III)

mineral, within the iron storage protein ferritin.¹⁸ However, examination of AD tissue has revealed increased proportions of iron(II)-containing biominerals such as magnetite and wüstite, when compared to disease-free control tissue.^{19–23} Both magnetite and wüstite have been demonstrated to be redox-active through their ability to partake in the Fenton reaction.²⁴ The reductive capacity of magnetite has also been exploited to convert chromium(VI) cations to chromium(III) cations in solution.^{25,26} Therefore, the presence of such redox-active iron phases in the brain could induce the production of ROS, resulting in oxidative stress. As oxidative damage is an early event in the development of AD, the presence of redox-active iron biominerals may be fundamental to AD pathogenesis.²⁷

Although the origin of these redox-active biominerals is unclear, evidence indicates their formation may involve the interaction of $A\beta$ with unbound brain iron, or the malfunction of the storage protein ferritin via the disruption of its oxidative function.^{21,28–31} Spectrophotometric studies conducted by Khan et al. show $A\beta$ to be capable of altering iron valence

Received: September 23, 2013

Published: February 21, 2014

chemistry, reducing iron(III) in solution to a divalent (Fe^{2+}) form.³² This coupled with the increased levels of iron previously found within amyloid plaque material³³ suggests a mechanism whereby $\text{A}\beta$ sequesters iron(III) forms before reducing them to iron(II) minerals.^{21,34,35} Indeed, electron tomography of amyloid plaque material obtained from AD brains provided evidence of ferritin core-sized iron oxide particles with a magnetite-like crystal structure.²¹ Furthermore, comparisons of pathological ferritin cores removed from AD tissue, to physiological ferritin, using nanoelectron diffraction, showed increased yields of both magnetite and a cubic mineral consistent with the iron(II) mineral wüstite, concurrent with lower yields of ferrihydrite.²⁸ This could suggest that ferrihydrite can be converted to iron(II)-bearing minerals as part of the disease process.

Despite these observations, the result of $\text{A}\beta$ interaction upon natural iron forms remains unknown, and the mineral products of this interaction have not been determined. In this study, synchrotron-based X-ray spectroscopy techniques were employed to examine the interaction between the AD peptide $\text{A}\beta$ and 2-line ferrihydrite. X-ray absorption spectroscopy (XAS) and X-ray magnetic circular dichroism (XMCD) are element-specific techniques that probe the oxidation state, site symmetry, and magnetic moments of -3d transition-metal ions in a composite material.^{36,37} XAS was utilized to detect changes in the oxidation state of ferrihydrite when incubated with $\text{A}\beta$ over a 144-h period, while simultaneous XMCD measurements probed changes in the magnetic properties and cation distributions of the iron mineral.

Using these techniques, both the detection of ferrihydrite chemical reduction by $\text{A}\beta$ and the characterization of any reduced iron forms were achieved. Furthermore, microstructural and phase analysis of $\text{A}\beta$ /ferrihydrite structures was obtained via transmission electron microscopy (TEM) and scanning transmission X-ray microscopy (STXM). These measurements were supported by iron(II) quantification assays to evaluate the proportion of ferrihydrite reduced by $\text{A}\beta$. Together, these approaches allowed the identification of iron species formed from the interaction of $\text{A}\beta$ with ferrihydrite while also quantifying the reductive capacity of $\text{A}\beta$, in an attempt to determine the origin of pathological iron forms found in AD tissue.

MATERIALS AND METHODS

Ferrihydrite Synthesis. Ferrihydrite particles were synthesized by neutralizing 100 g/L iron(III) chloride solution to pH 7 using 10 M sodium hydroxide (NaOH). The resulting ferrihydrite suspension was centrifuged at 10 000 rpm for 20 min and all of the supernatant was removed. This centrifugation process was repeated six times by repeatedly suspending the ferrihydrite particles in deionized water and removing the supernatant.³⁸

Preparation of β -Amyloid/Ferrihydrite Solutions. Ferrihydrite solutions (440 μM) were prepared from a ferrihydrite stock diluted with deionized water.

Monomeric synthetic $\text{A}\beta(1-42)$ (Bachem) was dissolved in 0.1 M NaOH to create a 220 μM $\text{A}\beta$ stock solution. This $\text{A}\beta$ stock was allowed to sit for 30 min to ensure complete peptide dissolution, before being added immediately to the 440 μM ferrihydrite solution. Ferrihydrite solutions were sonicated for 5 min prior to the addition of the $\text{A}\beta$ stock ensuring uniform ferrihydrite particle distribution. $\text{A}\beta$ /ferrihydrite solutions were neutralized to pH 7 with 0.5 M hydrochloric acid (HCl). Final

$\text{A}\beta$ and metal concentrations were 35 μM and 370 μM , respectively. $\text{A}\beta$ /ferrihydrite solutions were incubated at 37 °C until the time of sampling. $\text{A}\beta$ -free ferrihydrite controls were created as stated above by substituting deionized water for $\text{A}\beta$.

X-ray Absorption and X-ray Magnetic Circular Dichroism Spectroscopy. Fifteen (15) μL of $\text{A}\beta$ /ferrihydrite solutions (and their $\text{A}\beta$ -free controls) were pipetted onto carbon/Formvar-coated copper TEM grids (Agar Scientific) and excess liquid was removed, which allowed $\text{A}\beta$ /ferrihydrite aggregates to deposit without artifacts from the drying of the solution. Sampling was performed under anoxic conditions after 30 min, 48 h, and 144 h of incubation at 37 °C. The TEM grids were mounted onto copper plates for X-ray spectroscopy investigations, and kept under anoxic conditions to prevent changes in iron oxidation state (see the Supporting Information for further anoxic methodology).

XAS and XMCD measurements were performed on $\text{A}\beta$ /ferrihydrite samples, and their $\text{A}\beta$ -free controls using beamline I10 at the Diamond Light Source (Oxfordshire, U.K.), and Beamline 4.0.2 at the Advanced Light Source (Berkeley, CA). The XAS spectra of ferrihydrite was recorded using the total electron yield method. XMCD spectra were obtained by recording two XAS spectra with opposed magnetic fields orientated along the X-ray beam direction. To locate ferrihydrite accumulations, two-dimensional (2D) Fe maps at a spatial resolution of 100 μm were obtained (see Figure S1 in the Supporting Information). Detailed XAS and XMCD measurements across the Fe $L_{2,3}$ absorption-edge region (700–740 eV) were conducted on areas of ferrihydrite accumulation to study both the Fe oxidation and magnetic states. Not all grids provided regions of iron with sufficiently strong X-ray absorption signal to allow full XAS and XMCD analysis.

Quantification of Iron(II) in Solution: Ferrozine Assay. The iron(II) content of amyloid/ferrihydrite samples was quantified in solution using a Ferrozine colorimetric assay.³⁹ Ferrozine is a compound that selectively binds to iron(II) ions in solution, forming a magenta-colored solution upon iron binding. The intensity of this color is directly correlated to the concentration of iron(II) present, allowing the spectrophotometric quantification of iron(II) in solution.

To assess the iron(II) content of $\text{A}\beta$ /ferrihydrite and $\text{A}\beta$ -free ferrihydrite control incubations in solution, samples were digested in 0.5 M HCl for 3 h to release all bound iron from $\text{A}\beta$ structures. Digested samples were added to a 2 mM Ferrozine solution and absorbance read at 562 nm. The total iron content of samples was determined by concurrently reducing and digesting $\text{A}\beta$ /ferrihydrite and $\text{A}\beta$ -free ferrihydrite solutions over 3 h with 6.25 M hydroxylamine hydrochloride and 0.5 M HCl. Reduced samples were added to 2 mM Ferrozine, and absorbance read at 562 nm to provide total iron content values.

Iron(II) and total iron readings were taken after 0, 24, 48, 72, 120, and 144 h of incubation at 37 °C. No samples were taken at 96 h, because of limited sample volumes. Different $\text{A}\beta$ batches were used to the create $\text{A}\beta$ /ferrihydrite solutions for iron(II) quantification, and for XAS/XMCD measurements.

Statistical Analysis. Statistical analysis of iron(II) quantification data was conducted using a one-way analysis of variance (GraphPad Prism 6). This performs a hypothesis test of the equality of two or more population means. The null hypothesis of equal means was rejected at the 5% confidence level.

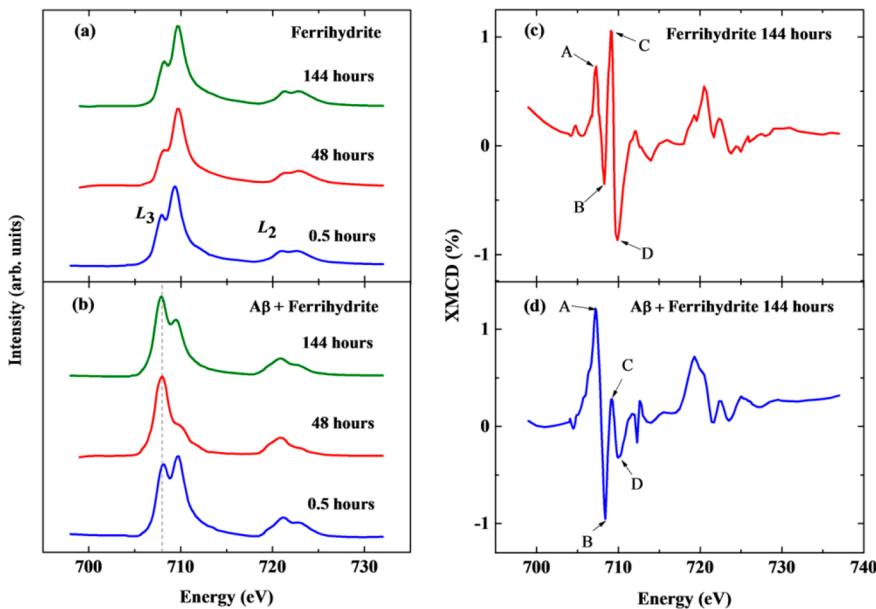


Figure 1. XAS spectra showing the Fe L-edge of ferrihydrite aggregates incubated (a) in the absence of $\text{A}\beta$ and (b) in the presence of $\text{A}\beta$. Incubation times are shown above the spectra. L_2 and L_3 regions are labeled in panel (a). The dashed gray line at 708 eV (panel (b)) shows the approximate position of the principle Fe^{2+} cation peak. Also shown are Fe $L_{2,3}$ -edge XMCD spectra of ferrihydrite aggregates after 144 h of incubation (c) in the absence of $\text{A}\beta$ and (d) in the presence of $\text{A}\beta$.

Transmission Electron Microscopy. Fifteen ($15\ \mu\text{L}$) $\text{A}\beta$ /ferrihydrite solutions and their $\text{A}\beta$ -free controls were dropped onto carbon/Formvar-coated copper TEM grids and the excess liquid was removed. Samples were taken after 30 min, 48 h, and 144 h of incubation at $37\ ^\circ\text{C}$ and examined using a transmission electron microscopy (TEM) system operating at 100 kV. These samples were not exposed to the X-ray beam used in XAS/XMCD.

Scanning Transmission X-ray Microscopy. $\text{A}\beta$ /ferrihydrite samples examined by XAS/XMCD were subsequently investigated using STXM on the PolLux Beamline at the Swiss Light Source (Villigen, Switzerland). STXM is a synchrotron-based technique for the imaging and the elemental analysis of a given structure to a spatial resolution of 20 nm, allowing the structure and composition of $\text{A}\beta$ /ferrihydrite aggregates to be visualized.

Sample TEM grids were mounted onto stainless steel plates for STXM examination and exposed to air throughout sample storage and transfer. Element-specific images displaying the carbon and iron content of amyloid aggregates were created by performing scans across the C K-edge (280–320 eV) and Fe $L_{2,3}$ -edges.

RESULTS

Fe $L_{2,3}$ XAS spectra obtained from ferrihydrite incubated in the presence and absence of $\text{A}\beta$ are shown in Figure 1, as a function of incubation time. From Figure 1a, the $\text{A}\beta$ -free ferrihydrite samples have XAS spectra characteristic of iron(III) minerals for all timing points, with a dominant peak at 709.5 eV and a low energy shoulder at 708 eV, both arising from Fe^{3+} cations (see iron(III) mineral reference spectrum in Figure 2a). The low-energy shoulder resides at the same energy as the Fe^{2+} cation dominant peak (see iron(II) chloride spectrum in Figure 2a). Thus increases in Fe^{2+} cation content manifest as an enhancement of this prepeak at 708 eV.

After 30 min of $\text{A}\beta$ /ferrihydrite incubation, XAS examination at the iron $L_{2,3}$ -edges (Figure 1b) showed the emergence of a

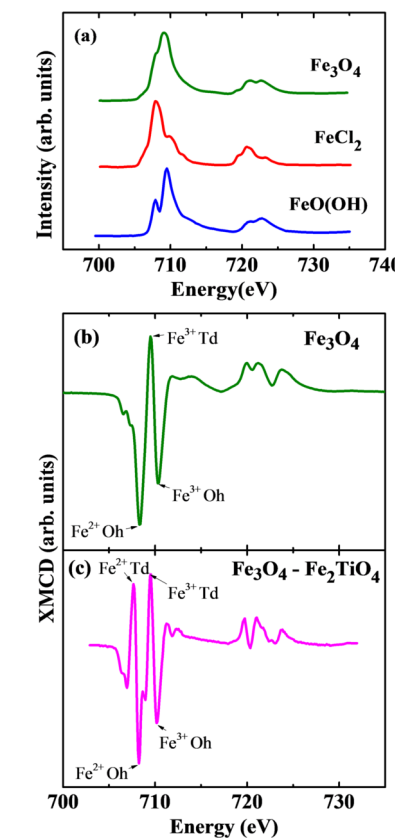


Figure 2. Fe $L_{2,3}$ absorption-edge XAS and XMCD reference spectra. (a) XAS spectra are shown, from bottom to top, for a pure iron(III) mineral (goethite, FeO(OH)), iron(II) chloride (FeCl_2), and magnetite (Fe_3O_4). (b) Magnetite (Fe_3O_4) XMCD spectrum with labeled octahedral (Oh) and tetrahedral (Td) Fe cation contributions. (c) Titanomagnetite XMCD spectrum with tetrahedral and octahedral Fe cation sites labeled (after ref 40).

significant Fe^{2+} cation component as evidenced by the enhanced 708 eV feature in comparison to $\text{A}\beta$ -free ferrihydrite (Figure 1a). Following 48 h of incubation with $\text{A}\beta$ (Figure 1b), ferrihydrite accumulations were found to be strongly reduced, with spectra closely resembling a pure iron(II) mineral (see Figure 2a). At this point, the Fe^{2+} cation peak at 708 eV becomes dominant, and the Fe^{3+} cation feature at 709.5 eV disappears. The effect is mirrored at the L_2 absorption region (720–725 eV).

Further incubation of $\text{A}\beta$ with ferrihydrite to 144 h (Figure 1b) led to the observation of a Fe^{2+} -cation-rich $\text{Fe}^{2+}/\text{Fe}^{3+}$ intermediate spectrum. Although oxidized in comparison to the pure iron(II) mineral observed after 48 h of incubation, ferrihydrite remained heavily reduced compared to $\text{A}\beta$ -free ferrihydrite controls (Figure 1a), with a large Fe^{2+} cation peak at 708 eV, followed by a smaller but distinct Fe^{3+} cation peak at 709.5 eV.

To confirm that these reduction effects were induced by $\text{A}\beta$, we assessed the impact of repeated X-ray beam exposure on the samples. We found only a subtle X-ray induced reduction effect in the $\text{A}\beta$ -free control samples (see Figure S2 in the Supporting Information). However, the 30 min $\text{A}\beta$ /ferrihydrite incubation sample appeared more susceptible to X-ray beam reduction, possibly due to destabilization of the ferrihydrite crystal structure by $\text{A}\beta$. Despite this, it was impossible to form pure iron(II) phases (Figure 1b) even after prolonged X-ray exposure (see Figure S3 in the Supporting Information).

The magnetic state of the samples was probed by XMCD across the $\text{Fe L}_{2,3}$ absorption edges. Magnetic minerals such as magnetite produce a strong XMCD effect of 10%–15%, with three prominent Fe L_3 -edge peaks corresponding to Fe^{2+} and Fe^{3+} cations occupying octahedral and tetrahedral crystal sites (see Figure 2b).^{40,41} For titanomagnetite, an additional positive peak is observed because of Fe^{2+} cations occupying tetrahedral sites (Figure 2c). The sign of the XMCD peaks (positive or negative) indicates the relative alignment of the magnetic moments of the cations. Furthermore, the different crystal symmetry at octahedral and tetrahedral sites results in a small energy shift in the XMCD peak positions for Fe^{3+} cations. Thus, although the opposing Fe^{3+} magnetic moments cancel each other, their presence can still be detected by XMCD.

The XMCD spectrum obtained from $\text{A}\beta$ -free ferrihydrite after 144 h incubation is shown in Figure 1c. At room temperature, ferrihydrite is expected to be in an antiferromagnetic or weakly ferrimagnetic state, with superparamagnetic properties due to the nanoscale crystal size.⁴² Here, we observe a small (1%–1.5%) XMCD effect and evidence of anti-ferromagnetic ordering of the cation moments, manifested as approximately equal intensity positive and negative peaks (labeled "A", "B", "C", and "D"). The clear energy separation of these peaks implies that the Fe cations occupy two non-equivalent crystal symmetry sites, similar to the tetrahedral and octahedral sites in magnetite. The relative intensities of the XMCD peaks in Figure 1c suggests the presence of predominantly Fe^{3+} cations (peaks C and D), with minor contributions from Fe^{2+} cations (peaks A and B). However, the XMCD spectrum obtained from the sample incubated with $\text{A}\beta$ (Figure 1d) shows a dramatic enhancement in the Fe^{2+} cation peaks (A and B), while preserving the anti-ferromagnetic ordering observed in the $\text{A}\beta$ -free ferrihydrite.

Hence, XMCD measurements confirm the iron reduction seen via XAS (Figure 1b), and they suggest the formation of an antiferromagnetically ordered iron(II) phase. It is possible that

this phase resembles the mineral wüstite (Fe_{1-x}O),^{43,44} although the antiferromagnetic order seen here would not be expected above the Néel temperature for wüstite (~200 K).

TEM and STXM images of $\text{A}\beta$ incubated with ferrihydrite are presented in Figure 3. TEM examination revealed $\text{A}\beta$

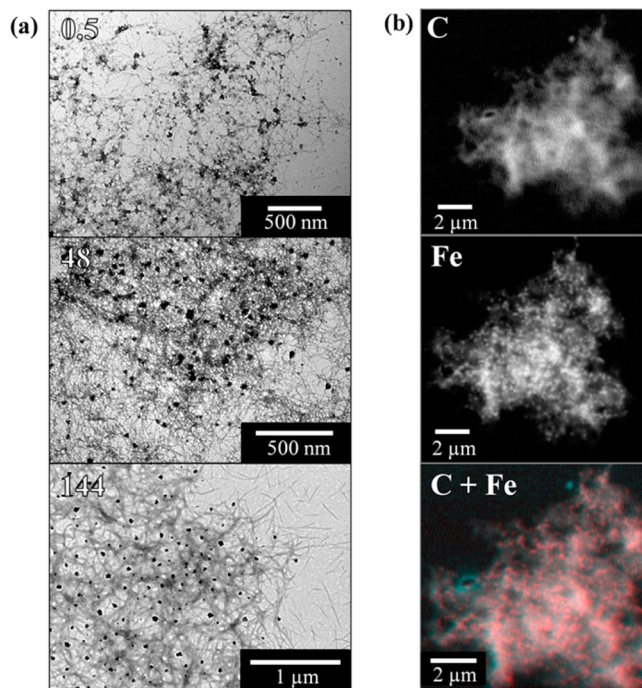


Figure 3. (a) Bright-field transmission electron microscopy (TEM) images and (b) scanning transmission X-ray microscopy (STXM) images of fibrillar amyloid structures formed following the incubation of $\text{A}\beta$ with ferrihydrite. TEM pictures show $\text{A}\beta$ structures present after 0.5, 48, and 144 h of incubation. STXM images show the carbon (C) and iron (Fe) content of an $\text{A}\beta$ /ferrihydrite aggregate, along with a carbon/iron (C + Fe) composite image of the same aggregate.

aggregates 1–50 μm in diameter, possessing fine fibril structure integrated with dense particles of ~50 nm across all time points examined (see Figure 3a).

To investigate the origin of the dense material within fibrillar $\text{A}\beta$ structures, we performed element-specific mapping of $\text{A}\beta$ /ferrihydrite aggregates incubated for 30 min using STXM. C K-edge and Fe L_3 -edge STXM images of an $\text{A}\beta$ /ferrihydrite aggregate are presented in Figure 3b. C K-edge examination revealed amyloid aggregates similar in nature to those pictured using TEM (Figure 3a). Corresponding Fe L_3 -edge STXM images showed the iron content to closely follow $\text{A}\beta$ morphology, suggesting integration and possible binding of the fine ferrihydrite particles with the $\text{A}\beta$ fibrils. In addition, larger, intense iron spots similar in size to the electron-dense particles shown in Figure 3a can be seen scattered throughout the $\text{A}\beta$ aggregate, suggesting that $\text{A}\beta$ acts to bind and accumulate ferrihydrite within its structure.

To further investigate the iron reduction capacity of $\text{A}\beta$, ferrihydrite solutions were incubated with $\text{A}\beta$ and their iron(II) content assessed by Ferrozine assay. The iron(II) content of $\text{A}\beta$ /ferrihydrite and $\text{A}\beta$ -free ferrihydrite solutions across the 144 h incubation time period are shown in Figure 4a.

Baseline iron(II) levels of the $\text{A}\beta$ -free ferrihydrite solutions remained constant throughout the time series, with no significant iron reduction being apparent. By examining control

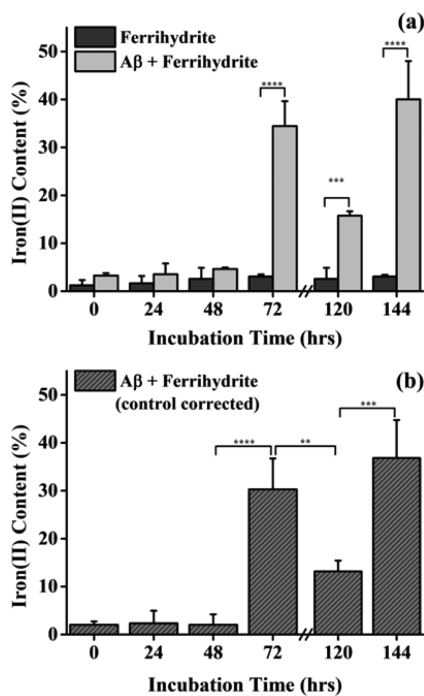


Figure 4. Ferrozine iron(II) quantification data showing iron(II) levels of $\text{A}\beta$ /ferrihydrite solutions over a 144-h incubation period: (a) iron(II) content as a percentage of total iron for ferrihydrite solutions in the absence (black) and presence (gray) of $\text{A}\beta$, and (b) control-corrected iron(II) content of $\text{A}\beta$ /ferrihydrite solutions, as a percentage of total iron. Sampling was not performed at 96 h of incubation. Error bars show the standard deviation ($n = 3$); statistically significant differences in mean values for each group comparison (by one-way analysis of variance (ANOVA)) are indicated by the following levels: (**) $p < 0.01$, (****) $p < 0.001$, (****) $p < 0.0001$.

corrected iron(II) levels of $\text{A}\beta$ /ferrihydrite solutions, a small iron(II) signal (2%) was observed over the first 48 h of incubation, before rising sharply to 30% after 72 h. Iron(II) levels then cycled, decreasing to 13% of total iron content at 120 h, then rising to 37% after 144 h of incubation.

These results confirm that $\text{A}\beta$ is capable of reducing ferrihydrite to an iron(II) form and suggest the establishment of an iron redox cycle. This redox cycling could explain why the pure iron(II) formed after 48 h of $\text{A}\beta$ /ferrihydrite incubation became oxidized following further incubation with $\text{A}\beta$ for 144 h (Figure 1b).

TEM images and selected area electron diffraction (SAED) patterns from $\text{A}\beta$ /ferrihydrite aggregates, $\text{A}\beta$ -free ferrihydrite controls and a magnetite reference are shown in Figure 5. $\text{A}\beta$ -free ferrihydrite was found to be 2-line in nature throughout all time points examined (Figure 5d), with broad reflections at 2.50 Å and 1.51 Å corresponding to the [110] and [300] reflections of ferrihydrite, respectively.⁴⁵

$\text{A}\beta$ /ferrihydrite aggregates examined at the 30-min and 144-h incubation time points provided diffraction patterns consistent with $\text{A}\beta$ -free ferrihydrite controls. However, analysis of $\text{A}\beta$ /ferrihydrite aggregates after 48 h of incubation revealed areas showing diffraction patterns with d -spacing values and reflection intensities reminiscent of a magnetite-like phase (JCPDS File Card No. 88-0315) (see Figures 5b–f). In areas of modest ferrihydrite accumulation (Figures 5b and 5d), weak diffraction rings were observed at 2.55, 2.11, 1.52, and 1.22 Å, corresponding to the [311], [400], [440], and [642] reflections of magnetite/maghemite, respectively. However, in areas of

extensive ferrihydrite accumulation (Figures 5c and 5e), stronger diffraction patterns were recorded with diffraction rings at 3.07, 2.55, 2.14, 1.8, 1.52, and 1.25 Å, corresponding to the [220], [311], [400], [422], [440], and [533/642] reflections of magnetite/maghemite, respectively. By comparing the diffraction pattern obtained from this $\text{A}\beta$ /ferrihydrite region to a magnetite reference (Figure 5f),⁴⁶ a clear correlation can be seen.

Magnetite is a strongly magnetic mineral, which is a feature that is not consistent with the XAS/XMCD results obtained from the iron(II) phase witnessed in the $\text{A}\beta$ /ferrihydrite series (Figure 1d). However, the magnetite seen in these diffraction patterns could represent the oxidation product of the iron(II) phase following air exposure.⁴⁷ The broad electron diffraction rings seen in Figures 5e and 5f suggest the nucleation and subsequent crystal growth of a nanocrystalline phase. This is consistent with the formation of a nanocrystalline Fe(II) phase from the ferrihydrite precursor and its subsequent oxidation to magnetite. This process is reminiscent of the synthetic nucleation and growth of ultrafine magnetite nanoparticles.⁴⁸ Complete oxidation of the Fe(II) mineral shown in Figure 1b, following prolonged air exposure, was confirmed by repeating the XAS measurements several months later (see Figure S4 in the Supporting Information).

DISCUSSION

From the use of X-ray absorption, iron(II) assay quantification, and TEM and STXM techniques, we show that the AD peptide $\text{A}\beta$ is capable of forming redox-active iron(II) minerals, following its aggregation with the ferric mineral ferrihydrite. XAS examination revealed an iron(II) phase to be formed following 48 h of $\text{A}\beta$ /ferrihydrite incubation. Concurrent XMCD analysis showed this phase to be weakly magnetic, with antiferromagnetically ordered moments, suggesting the formation of an iron(II) oxide such as wüstite.^{43,44} These findings are in agreement with 2004 work of Quintana et al., where a wüstite-like iron phase was observed within pathological AD ferritin.³⁰ The results presented here suggest $\text{A}\beta$ to be involved in the formation of the wüstite previously observed in pathological AD ferritin via reduction of ferrihydrite.³⁰ Iron(II) quantification assays showed evidence of ferrihydrite reduction in solution, supporting the data acquired via XAS, along with indications of ferrihydrite redox cycling by $\text{A}\beta$. Since a total iron content of 37% was found to be present in a divalent state (Fe^{2+}) and ferrihydrite was in a 10:1 excess to $\text{A}\beta$, these results indicate that $\text{A}\beta$ possesses a strong reductive capacity upon ferrihydrite.

Electron diffraction of $\text{A}\beta$ /ferrihydrite aggregates revealed the presence of an iron oxide consistent with magnetite. This is again in agreement with the Quintana et al. work, where an increased proportion of magnetite was observed within pathological ferritin;³⁰ along with results published by Pankhurst et al. in 2008²³ and Hautot et al. in 2003,²⁰ who reported increased magnetite levels in AD tissue, compared to disease-free controls. Since magnetite is the oxidation product of wüstite,⁴⁷ the mineral formed via $\text{A}\beta$ /ferrihydrite interaction may have oxidized to form magnetite when exposed to air during electron diffraction analysis. Furthermore, the fine nanoscale crystal size of the magnetite phase observed here is consistent with its formation from the ferrihydrite precursor, and could explain the origin of ferritin-core sized iron oxide nanoparticles with a magnetite/maghemite crystal structure

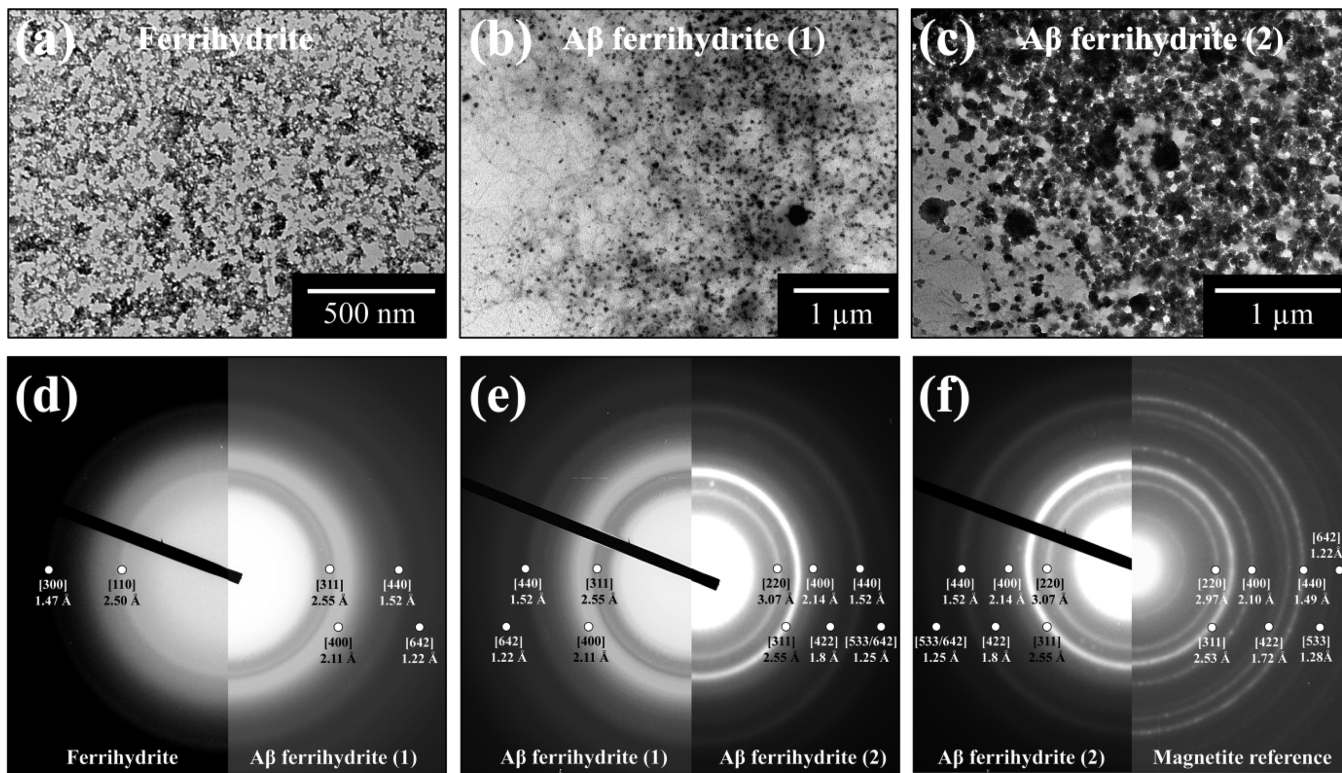


Figure 5. Transmission electron microscopy (TEM) images of ferrihydrite and A β /ferrihydrite aggregates, together with selected area electron diffraction (SAED) patterns obtained from these regions, following incubation for 48 h and subsequent air exposure: (a) TEM image of ferrihydrite in the absence of A β ; (b) TEM image of an A β /ferrihydrite aggregate in an area of modest ferrihydrite deposition; (c) TEM image of an A β /ferrihydrite aggregate in an area of extensive ferrihydrite deposition; (d) SAED pattern from ferrihydrite accumulations shown in panel (a), compared to A β /ferrihydrite aggregates shown in panel (b); (e) SAED patterns compared for A β /ferrihydrite aggregates shown in panels (b) and (c); and (f) SAED patterns compared for an A β /ferrihydrite aggregate shown in panel (c) and the magnetite reference.⁴⁶

witnessed within AD plaque cores (see the work of Collingwood et al.²¹).

STXM and TEM images suggest ferrihydrite particles integrate within A β fibril structures immediately after ferrihydrite addition, indicating an instantaneous interaction. In particular, STXM images show that A β is capable of both incorporating ferrihydrite into its structure, and concentrating ferrihydrite into larger clusters. These data strongly suggest that A β is capable of binding ferrihydrite (for A β /iron binding, see the 2009 work of Jiang et al.⁴⁹). It is this interaction that is thought to induce the reduction of ferrihydrite to an iron(II)-rich phase, following extended periods of contact with A β . On the basis of prior work by Huang et al.,¹⁷ we expect that the reduction of ferrihydrite by A β resulted in the oxidation of the peptide. Limitations of the techniques used here prevent confirmation of A β oxidation in the present study. It is also unclear whether the iron(II) phase formed via A β /ferrihydrite interaction represents a precursor to the magnetite previously seen in AD tissue, or whether magnetite could be formed independent of this intermediate phase.

Because iron is stored as redox-inactive ferrihydrite within the protein ferritin,¹⁸ the ability of A β to bind and reduce ferrihydrite into iron(II) phases that are known to be redox-active^{24–26} may play a key role in the pathogenesis of AD. Iron levels are high throughout the brain,¹⁰ with the stored iron form ferrihydrite being abundant. If ferritin function is compromised in AD tissues, exposure of ferrihydrite to A β is likely. The apparent efficiency at which A β can reduce ferrihydrite suggests this interaction would represent a

significant and sustained source of ROS capable of inducing widespread neuronal damage. In addition, with iron levels shown to be increased in areas of A β deposition in transgenic AD models overproducing A β ,⁵⁰ and in areas of AD pathology in post-mortem human AD tissue, the ability of A β to reduce ferrihydrite is likely to be a fundamental feature of AD pathology. We are subsequently exploring the interaction between A β and ferritin to determine the impact of A β on protein-bound ferrihydrite.

From this study, it is apparent that A β is directly capable of reducing synthetic ferrihydrite to pure iron(II) phases in the absence of any influencing factors. Because iron(II) phases do not occur naturally,^{28,30} these iron forms, which are associated with A β pathology, could represent a target for iron chelation therapies, intended to lower the ROS burden in neuronal tissue, thereby inhibiting the progression of AD. The formation of iron(II) oxides in this study also suggests a biogenic origin for the wüstite and magnetite previously recorded in AD tissue, providing insights into the processes of AD pathogenesis.

ASSOCIATED CONTENT

S Supporting Information

Description of anoxic sampling; two-dimensional X-ray absorption iron mapping (Figure S1); X-ray-beam-mediated iron reduction (Figures S2 and S3); and re-examination of oxidized iron(II) phases (Figure S4). This material is available free of charge via the Internet at <http://pubs.acs.org>.

AUTHOR INFORMATION

Corresponding Author

*Tel.: +44 (0)1782 555229. Fax: +44 (0)1782 674467. E-mail: n.d.telling@keele.ac.uk.

Author Contributions

†These authors contributed equally.

Author Contributions

The manuscript was written through contributions of all authors. All authors have given approval to the final version of the manuscript.

Notes

The authors declare no competing financial interest.

ACKNOWLEDGMENTS

This work was supported by Diamond Light Source, Ltd., and the EPSRC doctoral training grant (No. EP/P503981). This work was carried out with the support of the Diamond Light Source and we thank Dr. Peter Bencok for his assistance in the setting up of the beamline. The Advanced Light Source is supported by the Director, Office of Science, Office of Basic Energy Sciences, of the U.S. Department of Energy (under Contract No. DE-AC02-05CH11231). Measurements were also performed at the Swiss Light Source, Paul Scherrer Institute, Villigen, Switzerland, and we are grateful to the machine and beamline groups whose efforts have made these experiments possible. In particular, we would like to thank Dr. Joerg Raabe and Dr. Benjamin Watts for their support in setting up the beamline and the performing the experiment. We also thank Karen Walker (Keele University) for TEM support.

REFERENCES

- (1) Thompson, P. M.; Hayashi, K. M.; de Zubiray, G.; Janke, A. L.; Rose, S. E.; Semple, J.; Herman, D.; Hong, M. S.; Dittmer, S. S.; Doddrell, D. M.; Toga, A. W. *J. Neurosci.* **2003**, *23*, 994–1005.
- (2) Ong, W. Y.; Farooqui, A. A. *J. Alzheimer's Dis.* **2005**, *8*, 183–200.
- (3) Fox, N. C.; Crum, W. R.; Scachar, R. I.; Stevens, J. M.; Janssen, J. C.; Rossor, M. N. *Lancet* **2001**, *358*, 201–205.
- (4) Hardy, J.; Selkoe, D. J. *Science* **2002**, *297*, 353–356.
- (5) Hardy, J. A.; Higgins, G. A. *Science* **1992**, *256*, 184–185.
- (6) Fiala, J. C. *Acta Neuropathol.* **2007**, *114*, 551–571.
- (7) Rogers, J.; Morrison, J. H. *J. Neurosci.* **1985**, *5*, 2801–2808.
- (8) Goodman, L. *J. Nerv. Ment. Dis.* **1953**, *118*, 97–130.
- (9) Deibel, M. A.; Ehmann, W. D.; Markesberry, W. R. *J. Neurol. Sci.* **1996**, *143*, 137–142.
- (10) Connor, J. R.; Menzies, S. L.; Burdo, J. R.; Boyer, P. J. *Pediatr. Neurol.* **2001**, *25*, 118–129.
- (11) Munoz, P.; Humeres, A. *Biometals* **2012**, *25*, 825–835.
- (12) Smith, M. A.; Harris, P. L. R.; Sayre, L. M.; Perry, G. *Proc. Natl. Acad. Sci. U.S.A.* **1997**, *94*, 9866–9868.
- (13) Kell, D. B. *Arch. Toxicol.* **2010**, *84*, 825–889.
- (14) Bolt, H. M.; Marchant, R. *Arch. Toxicol.* **2010**, *84*, 823–824.
- (15) Honda, K.; Moreira, P. I.; Liu, Q.; Siedlak, S. L.; Zhu, X. W.; Smith, M. A.; Perry, G. *Lett. Drug Des. Discovery* **2005**, *2*, 479–482.
- (16) Smith, D. G.; Cappai, R.; Barnham, K. J. *Biochim. Biophys. Acta, Biomembr.* **2007**, *1768*, 1976–1990.
- (17) Huang, X. D.; Moir, R. D.; Tanzi, R. E.; Bush, A. I.; Rogers, J. T. *Ann. N.Y. Acad. Sci.* **2004**, *1012*, 153–163.
- (18) Chasteen, N. D.; Harrison, P. M. *J. Struct. Biol.* **1999**, *126*, 182–194.
- (19) Dobson, J. *Ann. N.Y. Acad. Sci.* **2004**, *1012*, 183–192.
- (20) Hautot, D.; Pankhurst, Q. A.; Khan, N.; Dobson, J. *Proc. R. Soc. B* **2003**, *270*, S62–S64.
- (21) Collingwood, J. F.; Chong, R. K. K.; Kasama, T.; Cervera-Gontard, L.; Dunin-Borkowski, R. E.; Perry, G.; Posfai, M.; Siedlak, S. L.; Simpson, E. T.; Smith, M. A.; Dobson, J. *J. Alzheimer's Dis.* **2008**, *14*, 235–245.
- (22) Collingwood, J. F.; Mikhaylova, A.; Davidson, M.; Batich, C.; Streit, W. J.; Terry, J.; Dobson, J. *J. Alzheimer's Dis.* **2005**, *7*, 267–272.
- (23) Pankhurst, Q.; Hautot, D.; Khan, N.; Dobson, J. *J. Alzheimer's Dis.* **2008**, *13*, 49–52.
- (24) Brillas, E.; Sires, I.; Oturan, M. A. *Chem. Rev.* **2009**, *109*, 6570–6631.
- (25) Telling, N. D.; Coker, V. S.; Cutting, R. S.; van der Laan, G.; Pearce, C. I.; Patrck, R. A. D.; Arenholz, E.; Lloyd, J. R. *Appl. Phys. Lett.* **2009**, *95*, 163701.
- (26) Cutting, R. S.; Coker, V. S.; Telling, N. D.; Kimber, R. L.; Pearce, C. I.; Ellis, B. L.; Lawson, R. S.; van der Laan, G.; Patrck, R. A. D.; Vaughan, D. J.; Arenholz, E.; Lloyd, J. R. *Environ. Sci. Technol.* **2010**, *44*, 2577–2584.
- (27) Nunomura, A.; Perry, G.; Aliev, G.; Hirai, K.; Takeda, A.; Balraj, E. K.; Jones, P. K.; Ghanbari, H.; Wataya, T.; Shimohama, S.; Chiba, S.; Atwood, C. S.; Petersen, R. B.; Smith, M. A. *J. Neuropathol. Exp. Neurol.* **2001**, *60*, 759–767.
- (28) Quintana, C.; Bellefqa, S.; Laval, J. Y.; Guerquin-Kern, J. L.; Wu, T. D.; Avila, J.; Ferrer, I.; Arranz, R.; Patino, C. *J. Struct. Biol.* **2006**, *153*, 42–54.
- (29) Quintana, C.; Gutierrez, L. *Biochim. Biophys. Acta* **2010**, *1800*, 770–782.
- (30) Quintana, C.; Cowley, J. M.; Marhic, C. *J. Struct. Biol.* **2004**, *147*, 166–178.
- (31) Dobson, J. *FEBS Lett.* **2001**, *496*, 1–5.
- (32) Khan, A.; Dobson, J. P.; Exley, C. *Free Radical Biol. Med.* **2006**, *40*, 557–569.
- (33) Lovell, M. A.; Robertson, J. D.; Teesdale, W. J.; Campbell, J. L.; Markesberry, W. R. *J. Neurol. Sci.* **1998**, *158*, 47–52.
- (34) Wan, L.; Nie, G.; Zhang, J.; Luo, Y.; Zhang, P.; Zhang, Z.; Zhao, B. *Free Radical Biol. Med.* **2011**, *50*, 122–129.
- (35) Castellani, R. J.; Moreira, P. I.; Liu, G.; Dobson, J.; Perry, G.; Smith, M. A.; Zhu, X. *Neurochem. Res.* **2007**, *32*, 1640–1645.
- (36) Regan, T. J.; Ohldag, H.; Stamm, C.; Nolting, F.; Luning, J.; Stohr, J.; White, R. L. *Phys. Rev. B* **2001**, *64*, 214422.
- (37) van der Laan, G. *J. Phys.: Conf. Ser.* **2013**, *430*, 012127.
- (38) Lovley, D. R.; Phillips, E. J. P. *Appl. Environ. Microbiol.* **1986**, *51*, 683–689.
- (39) Stookey, L. L. *Anal. Chem.* **1970**, *42*, 779–781.
- (40) Pearce, C. I.; Henderson, C. M. B.; Telling, N. D.; Patrck, R. A. D.; Charnock, J. M.; Coker, V. S.; Arenholz, E.; Tuna, F.; van der Laan, G. *Am. Mineral.* **2010**, *95*, 425–439.
- (41) Coker, V. S.; Gault, A. G.; Pearce, C. I.; van der Laan, G.; Telling, N. D.; Charnock, J. M.; Polya, D. A.; Lloyd, J. R. *Environ. Sci. Technol.* **2006**, *40*, 7745–7750.
- (42) Michel, F. M.; Barron, V.; Torrent, J.; Morales, M. P.; Serna, C. J.; Boily, J. F.; Liu, Q. S.; Ambrosini, A.; Cismas, A. C.; Brown, G. E. *Proc. Natl. Acad. Sci. U.S.A.* **2010**, *107*, 2787–2792.
- (43) Gheisari, M.; Mozaffari, M.; Acet, M.; Amighian, J. *J. Magn. Magn. Mater.* **2008**, *320*, 2618–2621.
- (44) Hazen, R. M.; Jeanloz, R. *Rev. Geophys.* **1984**, *22*, 37–46.
- (45) Janney, D. E.; Cowley, J. M.; Buseck, P. R. *Am. Mineral.* **2000**, *85*, 1180–1187.
- (46) Muller, K.; Skepper, J. N.; Posfai, M.; Trivedi, R.; Howarth, S.; Corot, C.; Lancelot, E.; Thompson, P. W.; Brown, A. P.; Gillard, J. H. *Biomaterials* **2007**, *28*, 1629–1642.
- (47) Park, J. C.; Kim, D.; Lee, C. S.; Kim, D. K. *Bull. Korean Chem. Soc.* **1999**, *20*, 1005–1009.
- (48) Iwasaki, T.; Sato, N.; Nakamura, H.; Watano, S. *Mater. Chem. Phys.* **2013**, *140*, 596–601.
- (49) Jiang, D.; Li, X.; Williams, R.; Patel, S.; Men, L.; Wang, Y.; Zhou, F. *Biochemistry* **2009**, *48*, 7939–7947.
- (50) Gallagher, J. J.; Finnegan, M. E.; Grehan, B.; Dobson, J.; Collingwood, J. F.; Lynch, M. A. *J. Alzheimer's Dis.* **2012**, *28*, 147–161.